# Ferromagnetic resonance damping mechanisms in CoFeB thin films with Cr substitution

Christian Lacroix [1,*] Kaan Oguz [2] John Michael David Coey [2] and David Ménard [1,†]

[1]*Department of Engineering Physics, Polytechnique Montréal, Montreal, Quebec, Canada H3T 1J4*
[2]*School of Physics, Trinity College, Dublin 2, Ireland*

The substitution of iron atoms by chromium in CoFeB films has been proposed to reduce the critical current density $J_c$ for current-driven magnetization switching in spin transfer torque devices by reducing its magnetization. Yet the effect of Cr on the magnetic damping has remained elusive. Ferromagnetic resonance (FMR) measurements up to 110 GHz and 5 T, as well as angle-dependent FMR measurements at 9.5 and 17 GHz, are used to discriminate between different mechanisms of FMR damping in $Co_{40}Fe_{40-x}Cr_xB_{20}$ thin films ($x = 0$, 4, 8, and 18). A constant isotropic Gilbert parameter is used to phenomenologically describe the magnetization damping for each composition, increasing from 0.005 to 0.022 as the amount of Cr increases from 0% to 18%. Two thirds of this contribution appear to be accounted for by intrinsic spin-orbit damping, and the balance is mostly due to extrinsic two-magnon scattering. While the introduction of Cr increases the spin-orbit damping, it nevertheless reduces the corresponding magnetic relaxation rate. The amorphous films with a high scattering rate exhibit a so-called conductivitylike damping at room temperature, in agreement with the breathing Fermi surface model. The presence of Cr also seems to inhibit internal fluctuations of the magnetization, reducing the two-magnon damping. The reduction of $J_c$ due to lower magnetization is partly mitigated by the overall increase in magnetic damping.

## I. INTRODUCTION

In the last 25 years, the emergence of spin-transfer-torque-based devices [1–3] and, more recently, magnonics devices [4] has led to a revival of interest in the magnetic damping of ferromagnets [5]. For instance, amorphous recrystallized CoFeB on a (001)-oriented MgO barrier allows for extremely large tunneling magnetoresistance [6,7]. As reported by Oguz *et al.* [8], chromium substitution for iron in the $Co_{40}Fe_{40}B_{20}$ free layer of a magnetic tunnel junction (MTJ) stack leads to a significant reduction of the saturation magnetization accompanied by a corresponding reduction of the critical current, inducing magnetization reversal through spin transfer torque. However, the effect of Cr substitution on the magnetic damping, which also determines the critical current, has remained elusive.

Over the last decade, magnetic damping in CoFeB has been intensively characterized [9–16]. It is generally accepted that a constant Gilbert term in the equation of motion can consistently describe a variety of intrinsic damping mechanisms due to the interaction of the spin system with the electron bath and the lattice [17]. Furthermore, other extrinsic contributions often play a significant, if not dominant, role in the magnetization dynamics.

Ferromagnetic resonance (FMR) [18,19] is widely used to investigate the magnetic damping, along with the crystallographic structure and the magnetic anisotropy in ferromagnets

[20,21]. In particular, field-swept FMR spectra as a function of frequency, magnetic field angle, or temperature can be exploited to discriminate between different mechanisms of magnetic losses, such as spin-lattice interactions, two-magnon scattering (TMS), inhomogeneous broadening, spin pumping, eddy currents, and radiation damping [22,23].

In this paper, we investigate the effect of Cr substitution on magnetic damping of $Co_{40}Fe_{40-x}Cr_xB_{20}$ films. Ferromagnetic resonance was measured as a function of frequency and field intensity as well as applied field direction. The measurements were carried up to 110 GHz with magnetic field up to 5 T to increase the accuracy. Analysis of the experimental data using known phenomenological models allowed us to evaluate quantitatively the strength of the intrinsic contributions to the damping as well as the extrinsic contributions, such as TMS, angular fluctuations of the internal field, and the spin-pumping contribution.

## II. EXPERIMENTAL DETAILS

### A. Film fabrication

Thin film stacks were prepared in a Shamrock sputtering system with a base pressure below $2.0 \times 10^{-8}$ Torr. Thin films of $Co_{40}Fe_{40-x}Cr_xB_{20}$ ($x = 0$, 4, 8, and 18) were deposited by cosputtering from high-purity (99.95%) $Co_{40}Fe_{40}B_{20}$ and $Co_{40}Cr_{40}B_{20}$ targets at room temperature on a $Si(001)/SiO_2(500$ nm$)/MgO(5$ nm$)$ stacking structure. A 5 nm thick Ta capping layer was added on top of the CoFeCrB layer. The thickness of the CoFeCrB films was nominally 30 nm. The thickness was chosen to ensure enough signal for

*christian.lacroix@polymtl.ca
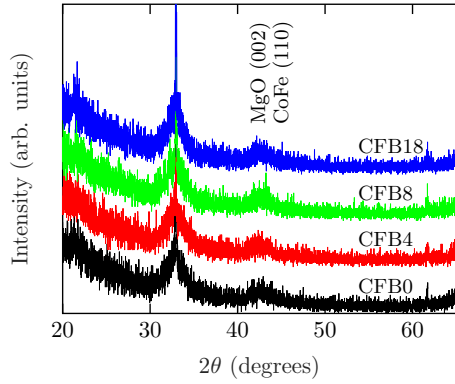†david.menard@polymtl.ca

FIG. 1. X-ray diffraction scans of CoFeCrB films with different Cr concentrations.

TABLE I. Physical properties of CoFeCrB films calculated from electrical characterization, magnetometry, and ferromagnetic resonance.

| Cr (%) | $\rho$ ($10^{-6}$ $\Omega$ m) | $M_s$ (MA/m) | $\mu_0 H_{\text{eff}}$ (T) | $K_s$ (kJ/m$^3$) | $g$ factor |
|---|---|---|---|---|---|
| 0 | 1.41 | $1.41 \pm 0.01$ | $1.55 \pm 0.02$ | $-152 \pm 5$ | $2.10 \pm 0.01$ |
| 4 | 2.31 | $0.87 \pm 0.01$ | $1.28 \pm 0.01$ | $81 \pm 2$ | $2.09 \pm 0.01$ |
| 8 | 2.54 | $0.72 \pm 0.01$ | $1.06 \pm 0.01$ | $58 \pm 2$ | $2.09 \pm 0.01$ |
| 18 | 2.99 | $0.21 \pm 0.01$ | $0.37 \pm 0.01$ | $11 \pm 1$ | $2.09 \pm 0.01$ |

the structural and magnetic characterization. The composition of the films was adjusted by carefully controlling the deposition rates of each target. High-purity (99.9999%) argon was used as the process gas, and the deposition pressure was kept at $6 \times 10^{-3}$ Torr. The samples were subsequently annealed at 350 °C for 1 h in high vacuum under a magnetic field of 0.8 T applied parallel to the sample plane. In what follows, four $Co_{40}Fe_{40-x}Cr_xB_{20}$ compositions are investigated, hereafter labeled CFB$x$, where $x = 0, 4, 8,$ and 18 corresponds to the atomic percentage of Cr.

### B. Structural characterization

The films were examined by x-ray diffraction (XRD) using Cu $K\alpha$ radiation. Figure 1 presents XRD $2\theta$ scans of the CoFeCrB films. After annealing at 350 °C, only the MgO (002) Bragg peak is observed (besides the Si substrate peaks). Other peaks, such as the CoFe (110) Bragg peak, are not observed, indicating that the films are amorphous.

Additional CoFeCrB films were fabricated and annealed at 400 °C instead of 350 °C. In the case of the CoFeB without Cr substitution, the presence of CoFe crystallites was confirmed through the observation of the CoFe 002 Bragg peak. This is compatible with previous works in which it was shown that the onset of crystallization occurs when CoFeB is annealed at above 370 °C for 1 h [24].

Finally, the thicknesses of the samples were verified using small-angle XRD scans. A thickness of 30 nm was found for all CoFeCrB films, as expected.

### C. Electrical properties

Electrical resistivity at room temperature, measured using a four-point method, is 1.41, 2.31, 2.54, and 2.99 $\times 10^{-6}$ $\Omega$ m for $x = 0, 4, 8,$ and 18 respectively (see Table I). These values, approximately one order of magnitude higher than those of well-known ferromagnetic metals such as Fe, Co, and Ni, are typical of amorphous metals. We note that the resistivity increases with Cr content.

### D. Magnetometry

Static magnetic properties were measured using an ADE Technologies vibrating sample magnetometer (model EV9).

Hysteresis curves of the CoFeCrB samples at 290 K, where the magnetic field is applied parallel to the plane of the sample, are presented in Fig. 2. In this configuration, there is practically no demagnetizing field. The coercive field and the saturation field are quite low, which is typical of a soft, amorphous, ferromagnetic material. We also observe that the saturation magnetization decreases as the content of Cr increases. The values of the saturation magnetization $M_s$ are reported in Table I.

## III. FERROMAGNETIC RESONANCE

FMR spectra were measured using a broadband shorted waveguide (SWG) technique [25] ranging from 27 to 110 GHz. It consists of positioning the sample on a "shorting" metallic plate placed at the end of a hollow $TE_{10}$ waveguide or, alternately, directly using the sample as the shorting plate. In this configuration, the sample is submitted to a maximum microwave magnetic field. Waveguides from the Ka band (WR28, 26.5–40 GHz), $V$ band (WR15, 50–75 GHz), and $W$ band (WR10, 75–110 GHz) were used. A microwave signal generator provided the microwave field up to 40 GHz. Two distinct microwave multipliers were used to generate frequencies for the $V$ and $W$ bands. The end of the waveguide (with the sample) was inserted in the bore of a 5 T superconducting magnet generating the static field, perpendicular to the microwave field. The reflected power from the SWG was recorded using microwave diodes as a function of the static
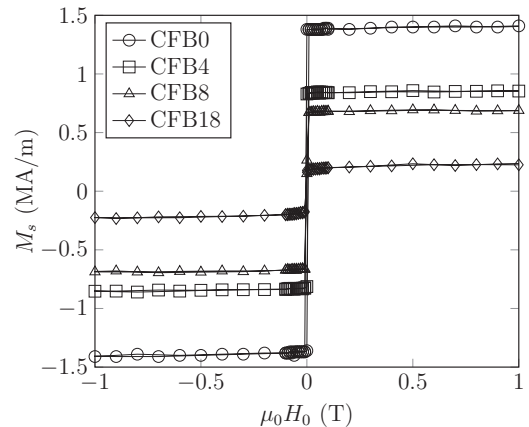


FIG. 2. Hysteresis curves of CoFeCrB films with different Cr concentrations obtained at 290 K. The magnetic field was applied parallel to the sample plane.
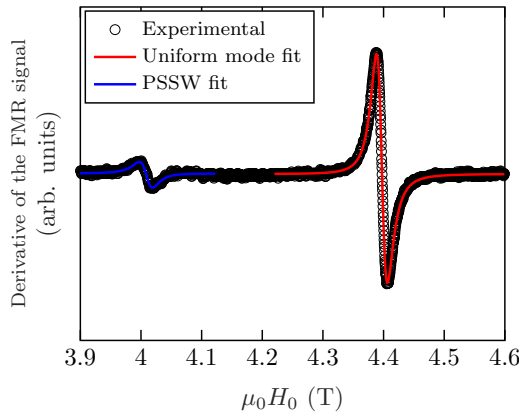
FIG. 3. FMR signal of sample CFB4 measured using the shorted waveguide technique at $f = 90.9$ GHz (circles). The magnetic field $H_0$ was applied perpendicular to the sample plane. The fits (lines) were obtained using the derivative of Eq. (1) with respect to $H_0$.

field. A field modulation scheme was enabled by an additional coil inserted in the bore to generate a small alternating field (1 mT, 100 Hz) parallel to the static field. A lock-in amplifier was used to detect the diode voltage, yielding the first derivative of the FMR spectrum. Frequency-dependent measurements were carried out with the static magnetic field applied both parallel (in plane) and perpendicular (out of plane) to the sample plane.

The angle-dependent measurements were carried out in a cavity setup. The samples were glued on a quartz rod to be positioned at the center of a $TE_{011}$ electromagnetic cavity, coupled to a waveguide. Two such resonators were used, with frequencies of 9.5 GHz in the $X$ band (WR-90) and 16.95 GHz in the Ku band (WR-75). The rod was parallel to the microwave magnetic field of the cavity. The 9.5 GHz cavity had a height of 45 mm and a radius of 20.5 mm. The 16.95 GHz cavity was 23 mm in height and had a radius of 11.5 mm. A vector network analyzer was used to excite the microwave cavity and measure its complex reflection coefficient over a frequency range around its resonant frequency. The variation of the amplitude of the reflection coefficient at the resonant frequency of the cavity was proportional to the imaginary part of the sample magnetic susceptibility [26]. A step motor combined with a pulley system was used to rotate the quartz rod and vary the angle between the plane of the sample and the static magnetic field [27].

All FMR measurements were carried out at room temperature ($292 \pm 2$ K). The samples used were square or rectangular with 2–3 mm sides.

A FMR signal obtained with the shorted waveguide technique is presented in Fig. 3 (open circles). The FMR signal of sample CFB4 was measured at $f = 90.9$ GHz with the magnetic field applied perpendicular to the sample plane. The resonance peak at $\mu_0 H_0 = 4.4$ T corresponds to the uniform mode, while the resonance peak at $\mu_0 H_0 = 4$ T is a perpendicular standing spin wave (PSSW) mode.

The FMR signal can be fitted using [28]

$$\text{Intensity} = A_1 \left( \cos\phi \frac{1}{1+x^2} - \sin\phi \frac{x}{1+x^2} \right) + A_2, \quad (1)$$

where $x = 2(H_0 - H_{res})/\Delta H$, $H_0$ is the applied magnetic field, $H_{res}$ is the resonance field, $\Delta H$ is the linewidth (full width at half maximum), $A_1$ is used to adjust the intensity, $\phi$ is the mixing angle between the dispersive and absorptive components of the high-frequency susceptibility of the material, and $A_2$ represents the background signal. Mixing is expected and often observed in good electrical conductors. In Fig. 3, the derivative of Eq. (1) with respect to $H_0$ was used to fit the resonance peaks. Nonlinear regression analysis of the least-squares fit led us to estimate a standard uncertainty of 0.01 mT for the resonance field and of 0.04 mT for the linewidth (based on the representative spectrum in Fig. 3).

### A. Resonance field

The frequency as a function of the resonance field is presented in Fig. 4 for the uniform mode for a magnetic field applied in plane (open circles) and out of plane (open squares). The general behavior is that expected from Kittel's resonance condition, as discussed below. In Fig. 5, the angular dependence of the resonance field ($f = 16.95$ GHz) is presented as the field varies from in plane (0°) to out of plane (90°). In both Figs. 4 and 5, the out-of-plane resonance field at a given frequency is significantly higher than the in-plane field because it must compensate the demagnetizing field. The behavior exhibited is typical of a sample whose magnetic anisotropy is dominated by the demagnetizing fields.

The resonance condition $\omega_{res}$ is obtained from the free energy density $U$ [29,30],

$$\omega_{res} = \frac{\gamma}{M_s \sin\theta_0} \left[ \frac{\partial^2 U}{\partial\theta^2} \frac{\partial^2 U}{\partial\varphi^2} - \left( \frac{\partial^2 U}{\partial\theta \partial\varphi} \right)^2 \right]_{\theta_0,\varphi_0}^{1/2}, \quad (2)$$

where $\gamma = g\mu_B/\hbar$ is the gyromagnetic ratio, $\theta_0$ and $\varphi_0$ describe the equilibrium direction of the magnetization $\vec{M}$, $\theta$ and $\varphi$ describe the direction of the magnetization relative to the sample, and $M_s$ is the magnitude of $\vec{M}$.

For a ferromagnetic thin film with a uniaxial out-of-plane magnetic anisotropy, the free energy density $U$ can be expressed as the sum of the Zeeman energy density and a magnetic anisotropy energy term,

$$U = -\mu_0 M_s H_0 [\sin\theta \sin\theta_H \cos\varphi + \cos\theta \cos\theta_H]$$
$$+ K_{eff} \sin^2\theta (\cos^2\varphi + \sin^2\varphi), \quad (3)$$

where $\theta_H$ describes the direction of the magnetic field relative to the sample plane, $K_{eff} = \mu_0 M_s H_{eff}/2$, and $H_{eff}$ is an effective anisotropy field.

Since the CoFeCrB films are essentially amorphous, magnetocrystalline anisotropy is negligible. Therefore, the magnetic anisotropy originates mainly from its demagnetizing field (shape effect), along with an additional uniaxial anisotropy $K_s$, possibly a surface/interface anisotropy term. The effective anisotropy constant $K_{eff}$ is expressed as

$$K_{eff} = \frac{\mu_0 N M_s^2}{2} + K_s, \quad (4)$$

where $N$ is the demagnetizing factor. For thin films, a negative $K_s$ value favors the alignment of the magnetization in the direction perpendicular to the surface, while a positive
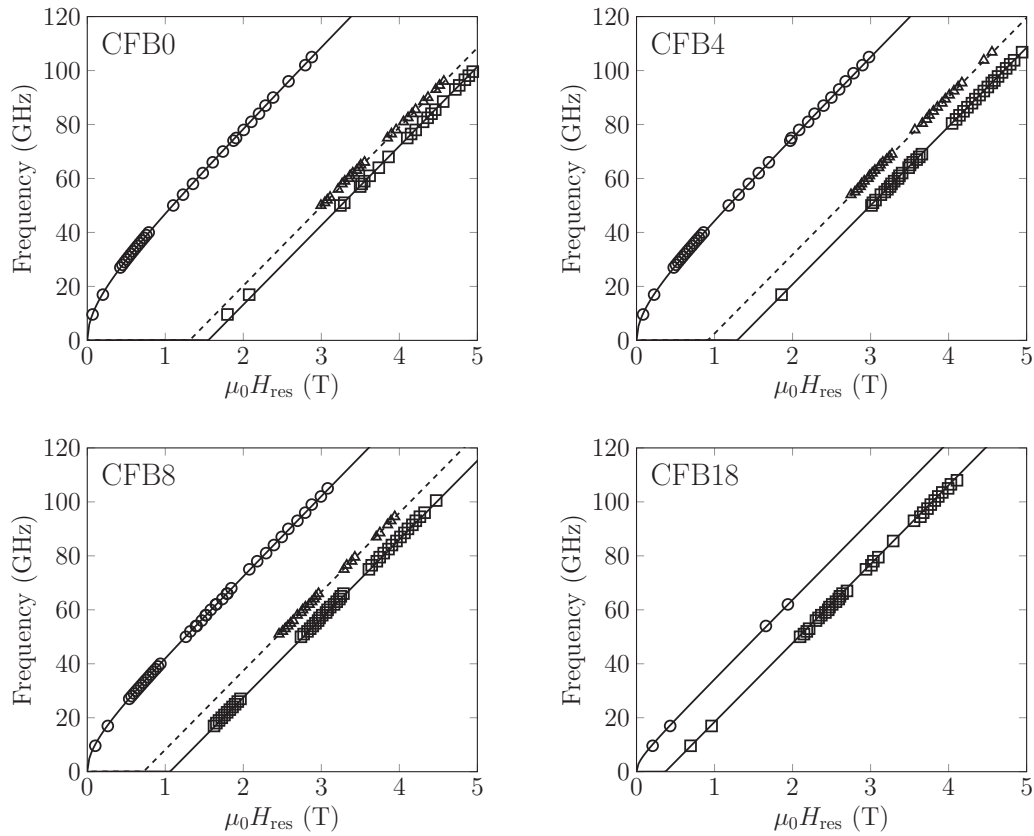
FIG. 4. Frequency of the uniform mode as a function of the resonance field $H_{res}$ applied in plane (circles) and out of plane (squares), along with the frequency of the first PSSW mode (triangles). For the uniform mode, the fits (solid lines) were calculated using Eq. (2). For the PSSW mode, the fits (dashed lines) were calculated using Eq. (13).

value favors the alignment of the magnetization parallel to the surface.

Minimizing the energy in Eq. (3) leads to the equilibrium position of the magnetization, which is then used in Eq. (2) to compute the frequency and angular dependences of the resonance field. The procedure leads to an excellent fit for the data for all samples (solid lines in Figs. 4 and 5). The values of the effective magnetic field $H_{eff}$ and $g$ factor that provide the best fit are summarized in Table I. The uncertainties were estimated by standard regression analysis.

Using $M_s$ values obtained from magnetometry and Eq. (4), $K_s$ was determined (see Table I). While $K_s$ is negative for CFB0 (no Cr), it is positive for CFB4, CFB8, and CFB18, indicating that there is a fundamental difference depending on whether Cr is present or not. Finally, we observe that the $g$ factor exhibits no clear dependence on the Cr content.

### B. Linewidth

The contributions to the linewidth (full width at half maximum) $\Delta H$ of the FMR signal can be expressed as

$$\Delta H = \Delta H_\alpha + \Delta H_\theta + \Delta H_{2m} + \Delta H_0, \qquad (5)$$

where $\Delta H_\alpha$ includes contributions proportional to the frequency, which are well described by a constant Gilbert parameter. In this term, we consider spin-orbit, spin-pumping, radiative, and eddy current damping. The term $\Delta H_\theta$ corresponds to the angular fluctuations of the sample magnetic

properties among various regions of the film, whereas $\Delta H_{2m}$ is the contribution originating from TMS processes. These last two terms are extrinsic because they relate to imperfections and inhomogeneities of the samples. The last term, $\Delta H_0$, is used to account for residual contributions that are frequency independent and angle independent and that are not included in the other terms.

The term $\Delta H_\alpha$ is quantified by the dimensionless parameter $\alpha$ and depends on the angle between the external applied field and the sample magnetization, which is expressed as [29]

$$\Delta H_\alpha = \frac{\alpha\gamma}{M_s(d\omega_{res}/dH_0)}\left(\frac{\partial^2 U}{\partial\theta^2} + \frac{\partial^2 U}{\partial\varphi^2}\frac{1}{\sin^2\theta}\right)_{\theta_0,\varphi_0}. \quad (6)$$

The term $\Delta H_\theta$ is due to the local fluctuations in the direction of the internal fields [31–33], that is,

$$\Delta H_\theta = \frac{\partial H_{res}}{\partial\theta_H}\Delta\theta, \qquad (7)$$

where $\Delta\theta$ is associated with the angular fluctuations of the internal field. This contribution reduces to zero when the external magnetic field is applied in plane or out of plane due to the derivative term in Eq. (7).

The TMS processes correspond to the transformation of a uniform magnon ($k = 0$) into two magnons having wave vectors $k \neq 0$. They are due to the presence of inhomogeneities [32], such as surface or interface defects [34], volume defects, and the presence of single-crystals grains [35]. In the case of a homogeneously magnetized thin film, the angular dependence
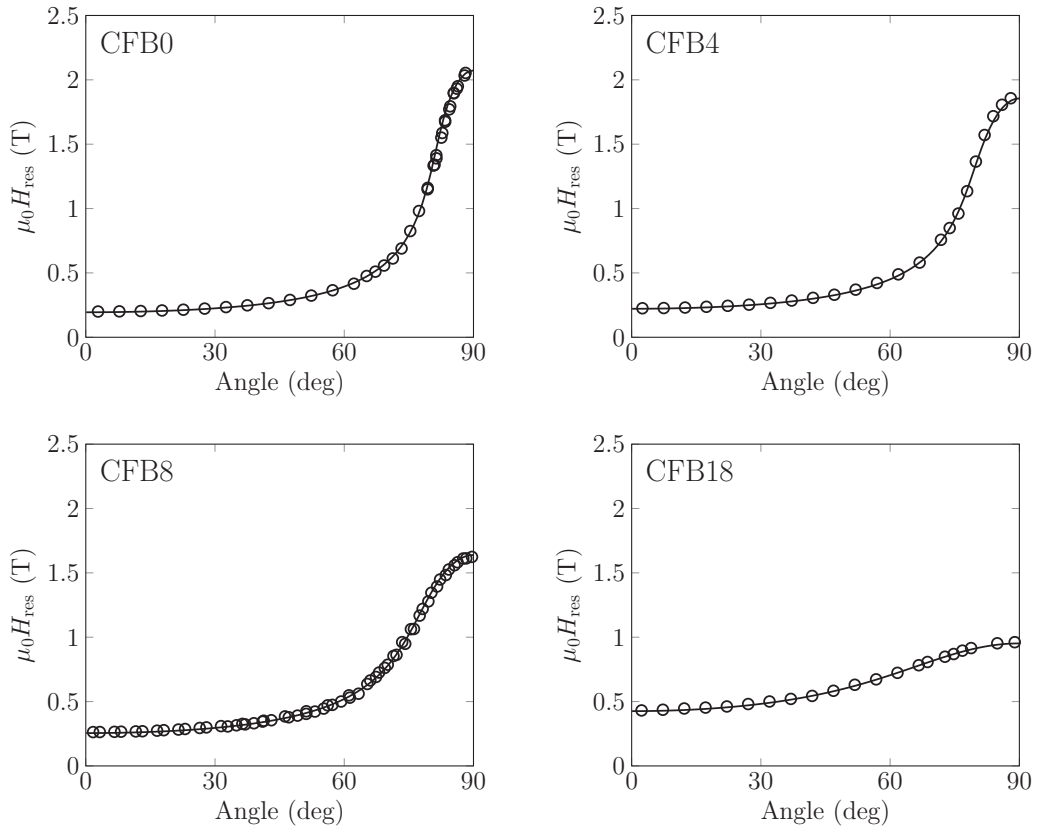
FIG. 5. Angular dependence of the resonance field $H_{res}$ of the uniform mode obtained at $f = 16.95$ GHz when the magnetic field direction is varied from the in-plane (0°) to the out-of-plane (90°) direction (circles). The fits (lines) were calculated using Eq. (2).

of the linewidth broadening $\Delta H_{2m}$ originating from TMS can be described as [22,36,37]

$$\Delta H_{2m} = \frac{\gamma \mu_0 \Gamma_0}{(d\omega_{res}/dH_0)} \, \mathrm{Re} \, \{\theta_c(\theta)\}, \qquad (8)$$

where

$$\theta_c(\theta) = \arcsin \sqrt{\frac{H_X}{H_X + H_{eff}} \frac{\cos(2\theta)}{\cos^2 \theta}}, \qquad (9)$$

$$H_X = H_0 \cos(\theta_H - \theta) - H_{eff} \sin^2 \theta, \qquad (10)$$

$$H_{eff} = \frac{2K_{eff}}{\mu_0 M_s}, \qquad (11)$$

and $\Gamma_0$ (in A/m) corresponds to the strength of TMS, assuming that $\Gamma_0$ is independent of $H_0$ and $\theta_H$ [38].

For a thin film with the static magnetic field applied out of plane, Eq. (6) reduces to $\Delta H_\alpha = 4\pi \alpha f_{res}/(\gamma \mu_0)$. In this configuration, TMS processes are ineffective [36], and $\Delta H_{2m}$ vanishes. Then, Eq. (5) reduces to [20]

$$\Delta H = \frac{4\pi \alpha}{\mu_0 \gamma} f_{res} + \Delta H_0, \qquad (12)$$

where $f_{res} = \omega_{res}/2\pi$. This configuration is very useful to obtain directly the magnetic damping parameter $\alpha$.

The frequency dependence of the linewidth, with the magnetic field applied in plane and out of plane, is presented in Fig. 6. For the out-of-plane data (squares), the linewidth varies almost linearly with the frequency with near-zero intercept for

all samples. The slope becomes smaller as the frequency is decreased, possibly due to the sample being not fully saturated at lower field. Our analysis is based on the assumption that all the magnetic moments are collinear within a single magnetically saturated domain. This can be difficult to achieve, especially in the out-of-plane configuration, due to strong demagnetizing fields. Therefore, only data above 75 GHz were fitted with Eq. (12) (dashed lines in Fig. 6) to increase the reliability.

Data for the in-plane configuration are also presented (circles in Fig. 6), except for sample CFB18 due to the lack of sensitivity of the setup. The linewidth is higher compared to that of the out-of-plane data and does not vary linearly with the frequency at low frequency. This behavior was observed elsewhere in the presence of TMS processes [22,39,40]. Assuming the presence of a TMS contribution to the linewidth modeled using Eq. (8), the experimental data for the in-plane configuration could be fitted using the $H_{eff}$ values from Table I and by adjusting $\Gamma_0$ (solid lines in Fig. 6).

The angular dependence of the linewidth, measured using a cavity operating at 16.95 GHz, is reported in Fig. 7. The linewidths are lowest for a field applied perpendicular to the sample plane ($\theta_H = 90°$) but strongly increase as the magnetic field is tilted away from the normal to the plane, as the angle between the magnetization and the applied magnetic field becomes significant, and then it diminishes as the magnetic field and the magnetization gradually align parallel to the sample plane.

The data were fitted assuming both Gilbert and TMS contributions to the linewidth. In the case of CFB0 (no Cr), an
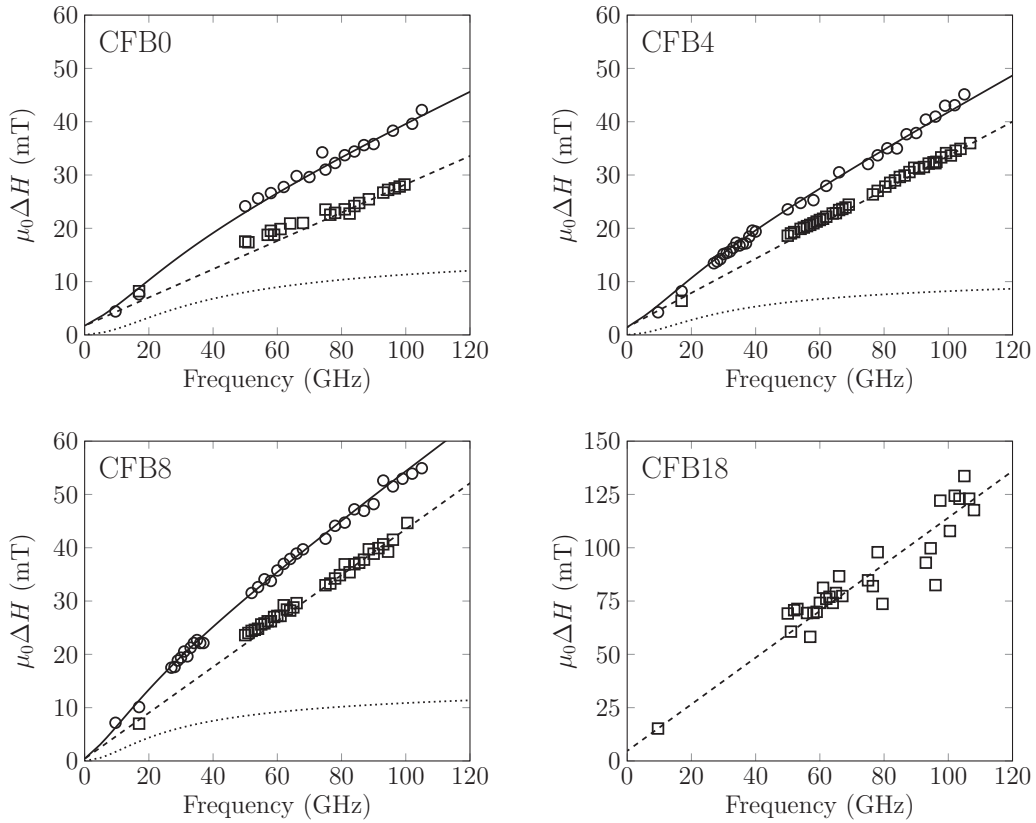
FIG. 6. Frequency dependence of the linewidth $\Delta H$ of the uniform mode when the magnetic field is applied out of plane (squares) and in plane (circles). The fits (solid black lines) were calculated using Eq. (5). The dashed lines correspond to $\Delta H_\alpha$, while the dotted lines correspond to $\Delta H_{2m}$.

additional contribution was required to account for angular fluctuations of the internal field [see Eq. (7)] [31]. Values used for the fits are presented in Table II along with those independently used to fit the data of Fig. 6. The uncertainties were estimated by standard regression analysis. The results from both frequency and angular measurement methods are in good agreement. The damping parameter $\alpha$ increases as the content of Cr increases. The results also indicate that $\Gamma_0$ is higher when the sample does not contain Cr, while it is quite similar for samples containing Cr.

### C. Perpendicular standing spin wave

Due to their relatively small thicknesses (30 nm), the films exhibit PSSWs [41]. An example of a PSSW measured on sample CFB4 is shown in Fig. 3 (the smaller peak at $\mu_0 H_0 = 4$ T). The PSSW signal can be fitted using the same

procedure as for the uniform mode based on Eq. (1). For a field applied perpendicular to the sample plane, assuming pinned spin boundary conditions for simplicity, the PSSW resonance condition is [19]

$$\omega_{\text{res}} = \gamma \mu_0 (H_0 - H_{\text{eff}} + H_{\text{ex}}), \qquad (13)$$

where $H_{\text{ex}}$ is the exchange field, which is related to the exchange stiffness constant $A_{\text{ex}}$ by

$$H_{\text{ex}} = \frac{2A_{\text{ex}}}{\mu_0 M_s} k_n^2, \qquad (14)$$

$k_n = (n\pi)/t$ is the spin-wave vector, $n$ is an integer, and $t$ is the thickness of the film [42,43].

The frequency dependence of the resonance field for the PSSW is presented in Fig. 4 (triangles) for samples CFB0, CFB4, and CFB8. Assuming $n = 1$ and fitting the

TABLE II. Parameters used to fit the linewidth of the uniform mode. The subscript "HF" indicates the parameters that were deduced from high-frequency measurements (above 75 GHz), while the subscript "17G" indicates the parameters that were deduced from the cavity-based setup operating at 16.95 GHz.

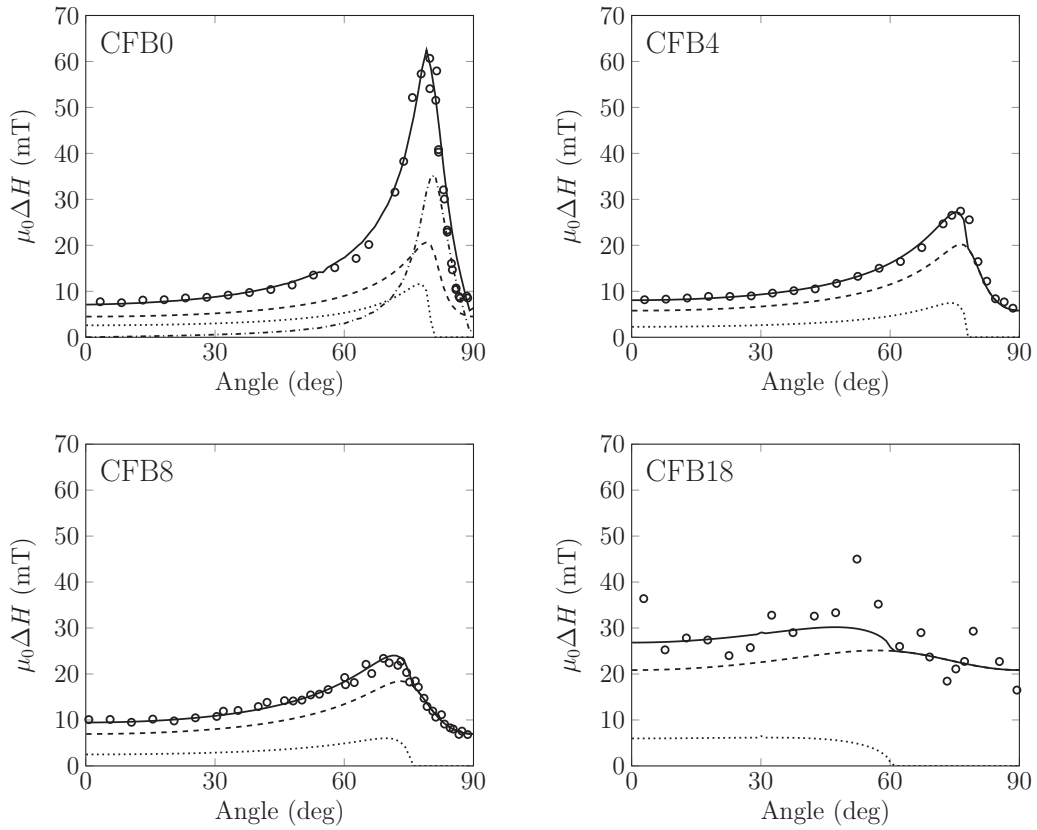| Cr (%) | $\alpha^{\text{HF}}$ ($10^{-3}$) | $\mu_0\Gamma_0^{\text{HF}}$ (mT) | $\mu_0\Delta H_0^{\text{HF}}$ (mT) | $\alpha^{\text{17G}}$ ($10^{-3}$) | $\mu_0\Gamma_0^{\text{17G}}$ (mT) | $\Delta\theta$ (deg) |
|---|---|---|---|---|---|---|
| 0 | $3.9 \pm 0.1$ | $12.6 \pm 0.4$ | $1.8 \pm 0.2$ | $3.9 \pm 0.4$ | $13 \pm 3$ | $0.25 \pm 0.05$ |
| 4 | $4.7 \pm 0.1$ | $8.5 \pm 0.2$ | $1.5 \pm 0.2$ | $5.0 \pm 0.1$ | $8.7 \pm 0.5$ | 0 |
| 8 | $6.3 \pm 0.1$ | $10.7 \pm 0.3$ | $0.4 \pm 0.1$ | $6.0 \pm 0.3$ | $7.5 \pm 0.8$ | 0 |
| 18 | $16 \pm 1$ | | $5 \pm 3$ | $18 \pm 4$ | $8 \pm 6$ | 0 |

FIG. 7. Angular dependence of the linewidth $\Delta H$ of the uniform mode when the magnetic field is rotated from the in-plane ($0°$) to the out-of-plane ($90°$) direction (circles). The fits (solid lines) were calculated using Eq. (5). The dashed lines correspond to $\Delta H_\alpha$, the dotted lines correspond to $\Delta H_{2m}$, and the dash-dotted lines correspond to $\Delta H_\theta$. Note that the experimental data could be well fitted using $\Delta H_0 = 0$.

experimental data with Eq. (13) yielded the $H_{ex}$ values reported in Table III. Using Eq. (14), the exchange stiffness constant was also calculated. The values are comparable to those measured previously for $Co_{40}Fe_{40}B_{20}$, for which values ranging between $1 \times 10^{-11}$ and $1.4 \times 10^{-11}$ J/m were reported [44]. One must keep in mind that these estimates could be modified depending on the nature of the spin boundary conditions (pinned or free or a mix of the two). The spin-wave stiffness parameter is expressed by $D_{sw} = 2A_{ex}g\mu_B/M_s$, which gives $D_{sw} = 4.3 \times 10^{-40}$ J m$^2$ for sample CFB0.

The frequency dependence of the PSSW linewidth (Fig. 8) was fitted using Eq. (12), yielding the Gilbert damping, here denoted $\alpha^{sw}$, and $\Delta H_0^{sw}$ (Table III). The $\alpha^{sw}$ values are similar to $\alpha^{HF}$ and $\alpha^{17G}$ obtained from the uniform mode. The extrinsic contribution to the PSSW linewidth $\Delta H_0^{sw}$ may originate from a small variation in the film thickness across the plane of the film [45].

TABLE III. Parameters extracted from the PSSW mode assuming pinned spin boundary conditions, with mode number $n = 1$.

| Cr (%) | $\mu_0 H_{ex}$ (T) | $A_{ex}$ ($10^{-11}$ J/m) | $\alpha^{sw}$ ($10^{-3}$) | $\mu_0 \Delta H_0^{sw}$ (mT) | $\Delta t$ (Å) |
|---|---|---|---|---|---|
| 0 | $0.24 \pm 0.01$ | $1.5 \pm 0.1$ | $3.1 \pm 0.4$ | $11 \pm 2$ | $7 \pm 1$ |
| 4 | $0.38 \pm 0.01$ | $1.5 \pm 0.1$ | $4.6 \pm 0.3$ | $9 \pm 2$ | $4 \pm 1$ |
| 8 | $0.34 \pm 0.01$ | $1.1 \pm 0.1$ | $6.0 \pm 0.6$ | $10 \pm 3$ | $4 \pm 1$ |

The broadening of the linewidth due to a variation in the film thickness can be calculated using

$$\Delta H_0 = \frac{2A_{ex}}{\mu_0 M_s} k_n^2 \frac{2\Delta t}{t}, \tag{15}$$

where $t$ is the film thickness and $\Delta t$ is the corresponding fluctuation in $t$.

The results indicate that a variation of a few angstroms in the film thickness, which corresponds to one or two atomic
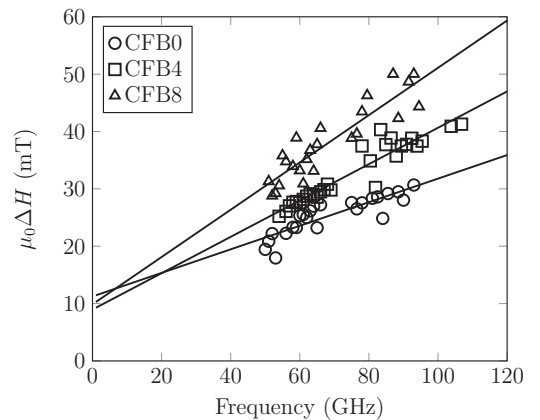


FIG. 8. Frequency dependence of the linewidth $\Delta H$ of the first PSSW model (symbols) for CFB0, CFB4, and CFB8. The lines are linear fits of the data.

TABLE IV. Calculated spin-pumping damping contribution due to the Ta layer $\alpha_{sp}$, spin-orbit damping ($\alpha_{so} = \langle \alpha \rangle - \alpha_{sp}$), and the corresponding magnetic relaxation rate $\lambda_{so}$.

| Cr (%) | $\alpha_{sp}$ ($10^{-3}$) | $\alpha_{so}$ ($10^{-3}$) | $\lambda_{so}$ ($10^9$ rad s$^{-1}$) |
|---|---|---|---|
| 0 | $0.5 \pm 0.1$ | $3.1 \pm 0.4$ | $1.0 \pm 0.1$ |
| 4 | $0.8 \pm 0.1$ | $4.0 \pm 0.2$ | $0.79 \pm 0.04$ |
| 8 | $1.0 \pm 0.1$ | $5.1 \pm 0.2$ | $0.83 \pm 0.03$ |
| 18 | $3.4 \pm 0.1$ | $14 \pm 2$ | $0.58 \pm 0.08$ |

layers, can explain the measured $\Delta H_0$. $\Delta t$ for all samples are given in Table III. It is found that $\Delta t$ deduced from sample CFB0 is almost twice that deduced from samples with Cr.

## IV. ANALYSIS AND DISCUSSION OF RESULTS

### A. Gilbert damping

Several contributions to the magnetic damping can be accounted for in the phenomenological Gilbert parameter $\alpha$. In ferromagnetic metals, the interaction between the magnetization and the macroscopic currents can be accounted for by simultaneously solving Maxwell's equations including the electrical currents (Ohm's law) and the Landau-Lifshitz-Gilbert equation of motion for the magnetization including the exchange field $H_{ex}$ [46]. These exchange conductivity effects become important whenever the effective skin depth is smaller than the thickness of the sample, which is not our case. For films thinner than the skin depth, it simply reduces to the well-known eddy current damping $\alpha_{ec}$, which leads to power dissipation proportional to frequency [47]. Another possible intrinsic contribution is the radiative damping $\alpha_{rad}$, which is related to the emission of microwave photons by precessing magnetic moments [48,49]. Those last two contributions ($\alpha_{ec}$ and $\alpha_{rad}$) are estimated to be less than 5% in the present case and will be disregarded hereafter.

Another mechanism is the damping enhancement due to spin pumping in the adjacent Ta layer $\alpha_{sp}$. It can be calculated from [5]

$$\alpha_{sp} = \frac{g_{eff}^{\uparrow\downarrow} \mu_B g}{4\pi M_s t},\tag{16}$$

where $g_{eff}^{\uparrow\downarrow}$ is the effective spin-mixing conductance. The value of $g_{eff}^{\uparrow\downarrow}$ for CoFeB/Ta bilayers measured experimentally was found to be $1.4 \times 10^{19}$ m$^{-2}$ [50]. The contribution of spin pumping $\alpha_{sp}$ is estimated and reported in Table IV.

The interaction of the magnetization with "microscopic currents" or "spin orbitals" is yet another intrinsic mechanism and was proposed 50 years ago [51]. This spin-orbit damping $\alpha_{so}$ is determined by subtracting $\alpha_{sp}$ from the averaged $\alpha$ values obtained experimentally, i.e., $\langle \alpha \rangle =$ mean($\alpha^{HF}$, $\alpha^{17G}$, $\alpha^{sw}$), in order to get the spin-orbit damping $\alpha_{so}$ (Table IV). The results indicate that the spin-orbit damping of CFB0 (no Cr) is close to 0.0031, which is in agreement with the $\alpha$ value reported in the literature for CoFeB ($\approx 0.004$) [9,11,15,33]. We note that $\alpha_{so}$ increases as the amount of Cr increases.
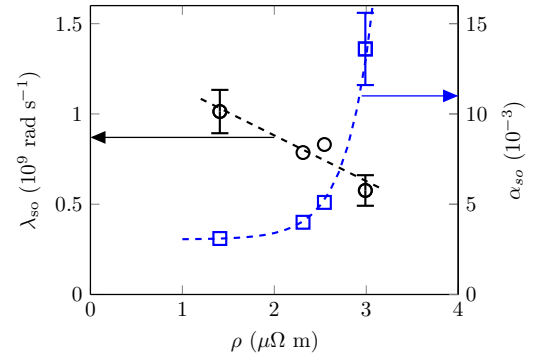


FIG. 9. Dependence of the magnetic relaxation rate $\lambda_{so}$ and the spin-orbit damping $\alpha_{so}$ on the electrical resistivity of the CoFeCrB films. The lines are guides for the eyes. When no error bar is present, the uncertainty is equal to or smaller than the size of the symbols.

### B. Spin-orbit damping

In ferromagnetic metals, it is recognized that the intrinsic damping is mainly caused by the itinerant nature of the electrons and the spin-orbit interaction [52]. In order to take into account the reduction in $M_s$ as the amount of Cr increases, the magnetic relaxation rate $\lambda_{so} = \gamma \mu_0 M_s \alpha_{so}$ is used instead of $\alpha_{so}$ to analyze the effect of Cr substitution. The magnetic relaxation rates $\lambda_{so}$ are reported in Table IV. For sample CFB0, $\lambda_{so}$ is similar to that found in the literature [33]. In contrast to $\alpha_{so}$, it is found that $\lambda_{so}$ diminishes as the content of Cr increases.

Kambersky's theory of magnetic damping in ferromagnetic metals predicts that the contribution from intraband transitions $\lambda_\sigma$ scales linearly with the electron relaxation time $\tau_e$ (conductivitylike behavior, which is also referred to in the literature as Kambersky's *breathing Fermi surface* theory), while the contribution from interband transitions $\lambda_\rho$ is inversely proportional to $\tau_e$ (resistivitylike behavior) [51,53]. The connection between the electrical resistivity and the magnetic relaxation rate has been demonstrated in transition metals theoretically and experimentally [23,54].

A larger amount of Cr in CoFeB appears to increase the disorder, as indicated by the increased electrical resistivity (Table I), but with a corresponding decrease of the magnetic relaxation rate, as shown in Fig. 9. This is consistent with the prediction of the breathing Fermi surface model, which can be interpreted as a reduced probability of intraband transitions associated with an increased structural disorder [23]. While a temperature-dependent FMR study would be very useful to further establish that connection, it is possible that the strong structural disorder maintains the "conductivitylike Gilbert damping" up to room temperature in our amorphous samples.

It is possible that Cr substitution also affects other parameters such as the lattice parameter and the density of states at the Fermi level, which could affect spin-orbit damping [55]. Finally, the decrease in $\lambda_{so}$ is opposite to the results reported by Fassbender *et al.* [56], who found that Cr content in NiFe films fabricated using ion implantation increases the magnetic relaxation rate. However, as discussed by Fassbender *et al.*, the sample preparation technique (ion implantation versus

TABLE V. Calculated theoretical defect area multiplied by the inhomogeneous stiffness field $A\langle\tilde{h}^2\rangle$ due to localized inhomogeneities [58] and the calculated theoretical two-magnon scattering contribution due to interface defects $\Gamma_{0,\text{surf}}$ [38].

| Cr (%) | $A\langle\tilde{h}^2\rangle$ $(10^{-7}$ A$^2)$ | $\mu_0\Gamma_{0,\text{surf}}$ ($\mu$T) |
|---|---|---|
| 0 | 1.40 | 671 |
| 4 | 1.43 | 101 |
| 8 | 1.35 | 85 |

cosputter deposition) likely plays a role in the magnetic relaxation rate.

### C. Two-magnon scattering

The second contribution to the linewidth in terms of importance is TMS. It results from the breaking of transitional symmetry; it is usually related to the presence of defects and imperfections [57]. Note that the two-magnon model can adequately reproduce the effect of small inhomogeneities, while large inhomogeneities are well described by the "local resonance" model [32].

A possible origin for TMS is the effects of localized inhomogeneities within the film such as variations in local magnetic properties (magnetization, magnetic anisotropy, etc.). In Ref. [58], Krivosik *et al.* described a Hamiltonian-based formalism to calculate linewidth enlargement due to TMS processes. Using Eq. (64) from Ref. [58], the quantity corresponding to $A\langle\tilde{h}^2\rangle$, where $A$ is the mean inhomogeneity area and $\langle\tilde{h}^2\rangle$ corresponds to the mean variation of the stiffness fields, was calculated (see Table V). The $A\langle\tilde{h}^2\rangle$ values obtained are very close to each other. Assuming a plausible mean inhomogeneity area $A$ of 50 nm$^2$, $\langle\tilde{h}\rangle \approx 7.5$ kA/m. This variation in the stiffness field could be due to, for example, spatial variation in the magnetization. In the case of sample CFB0, this would correspond to fluctuations in the magnetization of $\approx 0.5\%$. Such fluctuations in the magnetization could be induced by the fabrication process (sputtering deposition).

Another possible cause for TMS is the presence of interface roughness coupled to the presence of interface magnetic anisotropy [38]. At high field, the strength of the TMS processes due to interface roughness is given by $\Gamma_{0,\text{surf}} = 2H_s^2 b^2 p/(\pi D)$, where $H_s = 2K_s/(\mu_0 M_s)$, $b$ is the height (depth) of the islands (pits) at the interface, and $p$ is the fraction coverage of the defects (islands or pits). Assuming $p = 1$ and $b = \Delta t$ (see Table III), the values reported in Table V are obtained. Interestingly, the theory predicts that the TMS strength should be approximately one order of magnitude higher in sample CFB0 in comparison to CoFeCrB samples. This suggests that interface roughness can partially explain the higher TMS contribution in sample CFB0.

As reported in Table II, the TMS contribution is reduced when Cr is added to CoFeB. Furthermore, the linewidth broadening of sample CFB0 can be accounted for by angular fluctuations of the internal field in addition to TMS. This points to the presence of inhomogeneities in sample CFB0 that are suppressed when Cr is added. Furthermore, as mentioned earlier, the presence of CoFe crystallites was observed using XRD in CoFeB films annealed at 400 °C. It is possible that
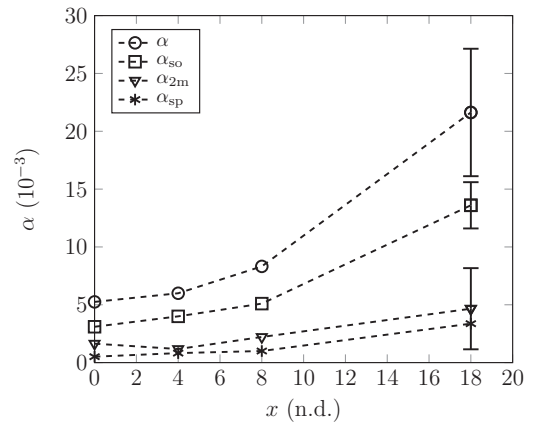


FIG. 10. Effect of Cr doping $x$ on the total damping $\alpha$, the spin-orbit damping $\alpha_{\text{so}}$, TMS damping $\alpha_{\text{2m}}$, and the spin-pumping damping $\alpha_{\text{sp}}$. The $\alpha_{\text{2m}}$ value is estimated assuming a magnetic field applied in the sample plane and a frequency of 16.95 GHz.

very small CoFe crystallites are also present in CoFeB films annealed at 350 °C, even if they were not detected in XRD scans, which could explain the higher TMS contribution and the angular fluctuations of the magnetic properties observed in sample CFB0. Another possible explanation is the reduction in the grain size due to the presence of Cr. Such amorphization was observed in permalloy doped with rare-earth atoms [59].

### D. Critical current density

The damping parameter $\alpha$ used in the equation of motion yields an expression for the critical current density for current-driven magnetization switching [3] $J_c \propto \alpha M_s(H_0 + H_{\text{eff}})/\eta$, where $\eta$ is the spin injection efficiency. For CoFeCrB films, considering that $H_{\text{eff}} \approx M_s$ and the applied magnetic field is low ($H_0 \ll H_{\text{eff}}$), $J_c \propto \alpha M_s^2/\eta$. In Fig. 10, the damping $\alpha$ is given for the case where a magnetic field is applied in the sample plane for different concentrations of Cr. It consists of the sum of three contributions: the spin-orbit ($\alpha_{\text{so}}$), TMS ($\alpha_{\text{2m}}$), and spin-pumping ($\alpha_{\text{sp}}$) contributions. Since TMS is not linear with the frequency, specifying the frequency at which $\alpha_{\text{2m}}$ is determined (16.95 GHz here) is required. Note that the main contribution is the spin-obit damping, which accounts for $\approx 60\%$–65% of the total damping.

According to Oguz *et al.* [8], the critical current density $J_c$ of a MTJ stack with $\text{Co}_{40}\text{Fe}_{40-x}\text{Cr}_x\text{B}_{20}$ as the free layer is reduced by a factor of 4 when $x = 7.3$, suggesting that the reduction in $J_c$ is mainly explained by the reduction in the saturation magnetization of the $\text{Co}_{40}\text{Fe}_{40-x}\text{Cr}_x\text{B}_{20}$ layer. Note that above $x = 10$, the coercivity is too low to obtain the bistable state required in spin torque transfer devices [8]. This calculation was done assuming that $H_{\text{eff}} \approx M_s$ and that $\alpha$ was unaffected by the presence of Cr. Using the $\alpha$ values from Fig. 10, the expected reduction in $J_c$ when $H_0$ is applied in the sample plane was calculated (Fig. 11). The reduction factor in $J_c$ when $x = 8$ is approximately 2.4, in agreement with the results from Ref. [60]. The main reason is that the decrease in $J_c$ originating from the reduced magnetization $M_s^2$ is partially compensated by the increased Gilbert damping parameter $\alpha$ as the content of Cr increases, as suggested earlier
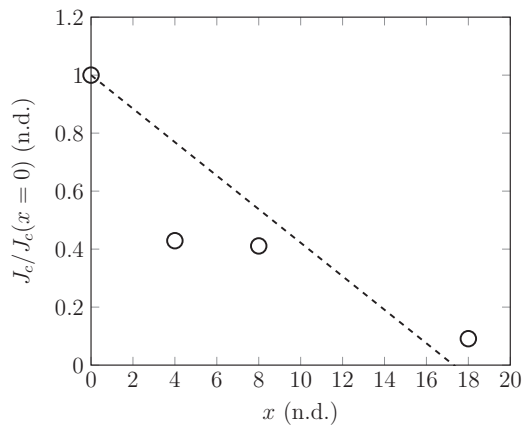
FIG. 11. Predicted reduction of critical current density for different Cr concentrations $x$. The line is a guide for the eyes. The uncertainty is equal to or smaller than the size of the symbols.

by Kubota *et al.* [60]. With the possibility of a further reduction in the critical current density, the spin-orbit damping is hard to eliminate. However, the possibility to reduce TMS by improving the fabrication process in order to eliminate spatial fluctuations in the magnetic properties remains. Eliminating TMS and spin-pumping contributions could thus allow the reduction of the total damping and the critical current density by $\approx$30–35%. Finally, in spin torque transfer devices, the thickness of the CoFeCrB layer is typically one order of magnitude smaller (3 nm vs 30 nm) [61]. The possible consequence is that a reduced thickness can modify the magnetic anisotropy [21]. On the other hand, the relative importance of a possible surface anisotropy term would scale as the inverse thickness. As for magnetic damping, it was reported that the spin-orbit damping is independent of the thickness, while the spin-pumping damping is inversely proportional to the thickness, as shown in Eq. (16). Furthermore, it is also expected that the TMS contribution originating from the interfacial magnetic anisotropy coupled to surface roughness will increase [38], while the TMS contribution from volume inhomogeneities will be independent of the thickness [58]. Hence, we expect that spin-pumping damping and surface TMS will increase as the film thickness is decreased and might become similar to spin-orbit damping and volume TMS [62].

## V. CONCLUSION

Ferromagnetic resonance spectroscopy on amorphous CoFeB films with Cr substitution allowed us to discriminate between different magnetic damping mechanisms. The presence of Cr reduces the magnetization, increases the electrical resistivity, and induces structural changes in the films that impact the magnetic anisotropy and magnetic damping of CoFeB. The magnetic relaxation rate of the spin-orbit damping decreases with an increasing amount of Cr, consistent with the prediction of the breathing Fermi surface model. It appears that our amorphous films with strong structural disorder exhibit a conductivitylike Gilbert damping at room temperature. A temperature-dependent study would be useful to further reinforce that conclusion.

Two-magnon scattering, which appears to be the main extrinsic contribution to the damping, is reduced due to the presence of Cr, suggesting a suppression of inhomogeneities in the samples. Two possible origins were investigated: volume and interface inhomogeneities. Calculations suggest that small spatial fluctuations ($\approx$0.5%) in the magnetization could explain most of the contribution, while interface roughness accounts for less than 5%. It is possible that these inhomogeneities in the magnetization correspond to some local ordering, which might act as nucleation centers for the growth of CoFe nanocrystals.

From an application point of view, the increased Gilbert damping when Cr is added to CoFeB partially cancels the gain obtained from the reduction in the magnetization. Considering that approximately one third of the damping originates from TMS, this suggests that the critical current density could be reduced by the same amount by eliminating inhomogeneities in the magnetization as well as interface roughness.

[1] J. Slonczewski, J. Magn. Magn. Mater. **159**, L1 (1996).

[2] L. Berger, Phys. Rev. B **54**, 9353 (1996).

[3] J. Z. Sun, Phys. Rev. B **62**, 570 (2000).

[4] A. Barman *et al.*, J. Phys.: Condens. Matter **33**, 413001 (2021).

[5] M. A. W. Schoen, D. Thonig, M. L. Schneider, T. J. Silva, H. T. Nembach, O. Eriksson, O. Karis, and J. M. Shaw, Nat. Phys. **12**, 839 (2016).

[6] Z. Diao, D. Apalkov, M. Pakala, Y. Ding, A. Panchula, and Y. Huai, Appl. Phys. Lett. **87**, 232502 (2005).

[7] S. Ikeda, J. Hayakawa, Y. Ashizawa, Y. M. Lee, K. Miura, H. Hasegawa, M. Tsunoda, F. Matsukura, and H. Ohno, Appl. Phys. Lett. **93**, 082508 (2008).

[8] K. Oguz, M. Ozdemir, O. Dur, and J. M. D. Coey, J. Appl. Phys. **111**, 113904 (2012).

[9] X. Liu, W. Zhang, M. J. Carter, and G. Xiao, J. Appl. Phys. **110**, 033910 (2011).

[10] H. Yu, R. Huber, T. Schwarze, F. Brandl, T. Rapp, P. Berberich, G. Duerr, and D. Grundler, Appl. Phys. Lett. **100**, 262412 (2012).

[11] A. Conca, J. Greser, T. Sebastian, S. Klingler, B. Obry, B. Leven, and B. Hillebrands, J. Appl. Phys. **113**, 213909 (2013).

[12] S. Iihama, S. Mizukami, H. Naganuma, M. Oogane, Y. Ando, and T. Miyazaki, Phys. Rev. B **89**, 174416 (2014).

[13] A. Ruiz-Calaforra, T. Bracher, V. Lauer, P. Pirro, B. Heinz, M. Geilen, A. V. Chumak, A. Conca, B. Leven, and B. Hillebrands, J. Appl. Phys. **117**, 163901 (2015).

[14] J. Cho, J. Jung, S.-Y. Cho, and C.-Y. You, J. Magn. Magn. Mater. **395**, 18 (2015).

[15] A. Okada, S. He, B. Gu, S. Kanai, A. Soumyanarayanan, S. T. Lim, M. Tran, M. Mori, S. Maekawa, F. Matsukura, H. Ohno, and C. Panagopoulos, Proc. Natl. Acad. Sci. USA **114**, 3815 (2017).

[16] B. Liu, D. Huang, M. Gao, H. Tu, K. Wang, X. Ruan, J. Du, J.-W. Cai, L. He, J. Wu, X. Wang, and Y. Xu, J. Magn. Magn. Mater. **450**, 65 (2018).

[17] V. Kambersky and C. E. Patton, Phys. Rev. B **11**, 2668 (1975).

[18] J. Griffiths, Nature (London) **158**, 670 (1946).

[19] C. Kittel, *Introduction to Solid State Physics*, 8th ed. (Wiley, Hoboken, NJ, 2004).

[20] B. Heinrich, in *Ultrathin Magnetic Structures*, edited by B. Heinrich and J. A. C. Bland (Springer, Berlin, 1994), Vols. 1–3.

[21] M. Farle, Rep. Prog. Phys. **61**, 755 (1998).

[22] J. Lindner, I. Barsukov, C. Raeder, C. Hassel, O. Posth, R. Meckenstock, P. Landeros, and D. L. Mills, Phys. Rev. B **80**, 224421 (2009).

[23] B. Khodadadi, A. Rai, A. Sapkota, A. Srivastava, B. Nepal, Y. Lim, D. A. Smith, C. Mewes, S. Budhathoki, A. J. Hauser, M. Gao, J.-F. Li, D. D. Viehland, Z. Jiang, J. J. Heremans, P. V. Balachandran, T. Mewes, and S. Emori, Phys. Rev. Lett. **124**, 157201 (2020).

[24] R. A. O'Dell, A. B. Phillips, D. G. Georgiev, J. G. Jones, G. J. Brown, and M. J. Heben, IEEE Trans. Magn. **54**, 1 (2018).

[25] I. Bady, IEEE Trans. Magn. **3**, 521 (1967).

[26] C. Lacroix, Propriétés magnétiques de nanoagrégats ferromagnétiques encastrés dans une épicouche semi-conductrice, Ph.D. thesis, École Polytechnique de Montréal, 2010.

[27] C. Lacroix, S. Lambert-Milot, R. A. Masut, P. Desjardins, and D. Ménard, Phys. Rev. B **87**, 024412 (2013).

[28] E. Montoya, T. McKinnon, A. Zamani, E. Girt, and B. Heinrich, J. Magn. Magn. Mater. **356**, 12 (2014).

[29] G. V. Skrotskii and L. V. Kurbatov, in *Ferromagnetic Resonance*, edited by S. V. Vonsovskii (Pergamon, Oxford, 1966), p. 12.

[30] A. G. Gurevich and G. A. Melkov, *Magnetization Oscillations and Waves* (CRC Press, Boca Raton, FL, 1996).

[31] C. Chappert, K. L. Dang, P. Beauvillain, H. Hurdequint, and D. Renard, Phys. Rev. B **34**, 3192 (1986).

[32] R. D. McMichael, D. J. Twisselmann, and A. Kunz, Phys. Rev. Lett. **90**, 227601 (2003).

[33] M. Oogane, T. Wakitani, S. Yakata, R. Yilgin, Y. Ando, A. Sakuma, and T. Miyazaki, Jpn. J. Appl. Phys. **45**, 3889 (2006).

[34] J. Lindner, K. Lenz, E. Kosubek, K. Baberschke, D. Spoddig, R. Meckenstock, J. Pelzl, Z. Frait, and D. L. Mills, Phys. Rev. B **68**, 060102(R) (2003).

[35] M. J. Hurben and C. E. Patton, J. Appl. Phys. **83**, 4344 (1998).

[36] P. Landeros, R. E. Arias, and D. L. Mills, Phys. Rev. B **77**, 214405 (2008).

[37] I. Barsukov, P. Landeros, R. Meckenstock, J. Lindner, D. Spoddig, Z.-A. Li, B. Krumme, H. Wende, D. L. Mills, and M. Farle, Phys. Rev. B **85**, 014420 (2012).

[38] R. Arias and D. L. Mills, Phys. Rev. B **60**, 7395 (1999).

[39] K. Zakeri, J. Lindner, I. Barsukov, R. Meckenstock, M. Farle, U. von Hörsten, H. Wende, W. Keune, J. Rocker, S. S. Kalarickal, K. Lenz, W. Kuch, K. Baberschke, and Z. Frait, Phys. Rev. B **76**, 104416 (2007).

[40] H. Kurebayashi, T. D. Skinner, K. Khazen, K. Olejnik, D. Fang, C. Ciccarelli, R. P. Campion, B. L. Gallagher, L. Fleet, A. Hirohata, and A. J. Ferguson, Appl. Phys. Lett. **102**, 062415 (2013).

[41] R. Weber, IEEE Trans. Magn. **4**, 28 (1968).

[42] J. M. D. Coey, *Magnetism and Magnetic Materials* (Cambridge University Press, Cambridge, 2009).

[43] M. A. W. Schoen, J. M. Shaw, H. T. Nembach, M. Weiler, and T. J. Silva, Phys. Rev. B **92**, 184417 (2015).

[44] J. Cho, J. Jung, K.-E. Kim, S.-I. Kim, S.-Y. Park, M.-H. Jung, and C.-Y. You, J. Magn. Magn. Mater. **339**, 36 (2013).

[45] G. C. Bailey and C. Vittoria, Phys. Rev. Lett. **28**, 100 (1972).

[46] W. S. Ament and G. T. Rado, Phys. Rev. **97**, 1558 (1955).

[47] J. M. Lock, Br. J. Appl. Phys. **17**, 1645 (1966).

[48] R. W. Sanders, D. Paquette, V. Jaccarino, and S. M. Rezende, Phys. Rev. B **10**, 132 (1974).

[49] G. Wende, Phys. Status Solidi A **36**, 557 (1976).

[50] D.-J. Kim, S.-I. Kim, S.-Y. Park, K.-D. Lee, and B.-G. Park, Curr. Appl. Phys. **14**, 1344 (2014).

[51] V. Kambersky, Can. J. Phys. **48**, 2906 (1970).

[52] B. Heinrich, in *Ultrathin Magnetic Structures III: Fundamentals of Nanomagnetism*, edited by B. Heinrich and J. A. C. Bland (Springer, Berlin, 2004), p. 143.

[53] M. Fähnle and C. Illg, J. Phys.: Condens. Matter **23**, 493201 (2011).

[54] K. Gilmore, Y. U. Idzerda, and M. D. Stiles, Phys. Rev. Lett. **99**, 027204 (2007).

[55] X. Ma, L. Ma, P. He, H. B. Zhao, S. M. Zhou, and G. Lüpke, Phys. Rev. B **91**, 014438 (2015).

[56] J. Fassbender, J. von Borany, A. Mücklich, K. Potzger, W. Möller, J. McCord, L. Schultz, and R. Mattheis, Phys. Rev. B **73**, 184410 (2006).

[57] M. Sparks, *Ferromagnetic Relaxation Theory* (McGraw-Hill, New York, 1964).

[58] P. Krivosik, N. Mo, S. Kalarickal, and C. E. Patton, J. Appl. Phys. **101**, 083901 (2007).

[59] W. Bailey, P. Kabos, F. Mancoff, and S. Russek, IEEE Trans. Magn. **37**, 1749 (2001).

[60] H. Kubota, A. Fukushima, K. Yakushiji, S. Yakata, S. Yuasa, K. Ando, M. Ogane, Y. Ando, and T. Miyazaki, J. Appl. Phys. **105**, 07D117 (2009).

[61] K. Oguz, Spin transfer torque magnetisation switching in MgO based magnetic tunnel junctions, Ph.D. thesis, Trinity College Dublin, 2010.

[62] Y. Li, C. Li, Q. Du, K. Shi, Z. Zhou, M. Liu, and J. Pan, J. Phys. D **55**, 245001 (2022).